Measurements of Cl-atom photofragment angular momentum distributions in the photodissociation of Cl_2 and ICl

T. Peter Rakitzis, S. Alex Kandel, Andrew J. Alexander, Zee Hwan Kim, and Richard N. Zare
Department of Chemistry, Stanford University, Stanford, California 94305

(Received 17 September 1998; accepted 11 November 1998)

We have studied the complete Cl-atom molecular-frame photofragment angular momentum distributions from the photodissociation of Cl_2 and ICl in the 320–560 nm region using time-of-flight mass spectroscopy with laser detection. The experimental signals were analyzed using the polarization-parameter formalism described in the preceding paper. These experiments study three distinct cases. The first case is the 470 nm dissociation of Cl_2 through the $B\,^3\Pi_{0^+u}$ state accessed via a parallel transition, yielding Cl-atom photofragments with polarizations described by the single parameter $\mathbf{a}_0^{(2)}(\parallel) = -0.7 \pm 0.2$. The second case is the 320 nm dissociation of Cl_2 through the $C\,^1\Pi_{1u}$ state accessed via a perpendicular transition, yielding Cl-atom photofragments with polarizations described by the two parameters $\mathbf{a}_0^{(2)}(\perp) = -0.50 \pm 0.10$ and $\mathbf{a}_2^{(2)}(\perp) = -0.32 \pm 0.06$. The third case is the dissociation of ICl in the 490–560 nm region in which dissociative states of both parallel and perpendicular character are accessed. In this wavelength region, the polarizations of the resulting Cl-atom photofragments are completely described by the approximately constant incoherent parameters, $\mathbf{a}_0^{(2)}(\parallel) \approx +0.4$, $\mathbf{a}_0^{(2)}(\perp) \approx -0.2$, and $\mathbf{a}_2^{(2)}(\perp) \approx -0.2$, whereas the interference contributions to the polarization, the $\mathrm{Im}[\mathbf{a}_1^{(1)}(\parallel,\perp)]$ and $\mathrm{Re}[\mathbf{a}_1^{(2)}(\parallel,\perp)]$, oscillate sinusoidally with excitation wavelength in a fashion that is sensitive to the shapes of the dissociative surfaces. © *1999 American Institute of Physics.* [S0021-9606(99)01707-9]

I. INTRODUCTION

Molecular photodissociation produces fragments that in general possess angular momentum. van Brunt and Zare[1] predicted that the photodissociation of molecules can, in certain cases, produce highly aligned angular momentum distributions. Recently, Eppink *et al.*[2] reported the production of maximally aligned $O(^1D)$ atoms, preferentially populating $m_J = 0$ with respect to the recoil direction, from the photodissociation of molecular oxygen. Measurements of maximal alignment are reported here in the angular momentum distributions of $Cl(^2P_{3/2})$ atoms from the photodissociation of Cl_2. These special cases correspond to single-surface adiabatic photodissociations. In general, however, photodissociations can proceed both adiabatically and nonadiabatically through multiple dissociative surfaces. For these more general cases, the photofragment angular momentum distributions can be more complicated.[3] The spatial distribution of the photofragment angular momentum is correlated to dynamically important vectors such as the recoil direction $\mathbf{v}$ and the transition dipole moment μ. This spatial distribution of angular momenta, measured with respect to $\mathbf{v}$ and μ, is rich in information about the dissociation process. The preceding paper[4] details methods for describing the photofragment angular momentum distribution in terms of just a few molecular-frame polarization parameters, the $\mathbf{a}_q^{(k)}(p)$.

The $\mathbf{a}_q^{(k)}(p)$ polarization parameters, closely related to the formalism used in the full quantum treatment of Siebbeles *et al.*,[3] each possess distinct physical significance. They decompose the angular momentum distributions into incoherent contributions from surfaces accessed by pure parallel and perpendicular transitions [the $\mathbf{a}_0^{(k)}(\parallel)$ and the $\mathbf{a}_0^{(k)}(\perp)$ and $\mathbf{a}_2^{(k)}(\perp)$ parameters, respectively], and into contributions from interference between surfaces of different symmetry [the $\mathbf{a}_1^{(k)}(\parallel,\perp)$ parameters]. The aim of this paper is to demonstrate the usefulness of the $\mathbf{a}_q^{(k)}(p)$ formalism by studying the UV and visible photodissociation of Cl_2 and ICl. In particular, we present three studies that appropriately illustrate the advantage of decomposing the photofragment angular momentum distributions into single-surface and multiple-surface contributions. These studies involve the complete measurement of the $Cl(^2P_{3/2})$ photofragment angular momentum distributions in the following cases: the pure parallel excitation of Cl_2 to the B state at 470 nm; the pure perpendicular excitation of Cl_2 to the C state at 320 nm; and the mixed excitation, of both parallel and perpendicular character, of ICl in the 490–560 nm range. These three examples represent the two limiting cases (pure parallel and perpendicular transitions) and one intermediate case of excitation symmetry. We show that in the case of pure-parallel excitation, the $Cl(^2P_{3/2})$ photofragment polarization is described by the $\mathbf{a}_0^{(2)}(\parallel)$ parameter only; in the case of pure-perpendicular excitation, the $Cl(^2P_{3/2})$ photofragment polarization is described by the $\mathbf{a}_0^{(2)}(\perp)$ and $\mathbf{a}_2^{(2)}(\perp)$ parameters only; and in the case of mixed excitation, the Cl $(^2P_{3/2})$ photofragment polarization is described by the three single-surface parameters mentioned above as well as the $\mathrm{Im}[\mathbf{a}_1^{(1)}(\parallel,\perp)]$ and $\mathrm{Re}[\mathbf{a}_1^{(2)}(\parallel,\perp)]$ multiple-surface interference terms.

The $\mathrm{Im}[\mathbf{a}_1^{(1)}(\parallel,\perp)]$ and $\mathrm{Re}[\mathbf{a}_1^{(2)}(\parallel,\perp)]$ interference terms are shown to be proportional to $\sin\Delta\phi$ and $\cos\Delta\phi$, respec-

tively, where $\Delta\phi$ is the asymptotic phase difference between the continuum wavefunctions associated with the two surfaces involved in the dissociation. The phase difference $\Delta\phi$ depends on the dissociation energy and photofragment mass in a fashion that is very sensitive to the shapes of the dissociative surfaces. As such, the wavelength-dependent measurement of these interference parameters can be used as a spectroscopy of multiple dissociative states. Wavelength-dependent oscillations in the photofragment alignment caused by multiple-surface interference have been observed in the electronically excited H $(2p)$ and D $(2p)$ photofragments resulting from the photodissociation of H_2 and D_2.[5,6] The oscillations observed in the total alignment are exclusively caused by the $\mathrm{Re}[\mathbf{a}_1^{(2)}(\parallel,\perp)]$ parameter. Recent work in this laboratory measured the orientation of the Cl $(^2P_{3/2})$ photofragments resulting from the photolysis of ICl with linearly polarized light.[7] In this case, the photofragment orientation is exclusively caused by the $\mathrm{Im}[\mathbf{a}_1^{(1)}(\parallel,\perp)]$ parameter.

Section II presents the experimental techniques used to obtain time-of-flight profiles from which the photofragment polarization parameters $\mathbf{a}_q^{(k)}(p)$ are extracted. Section III demonstrates simple methods to calculate the experimental sensitivities s_k to the $\mathbf{a}_q^{(k)}(p)$ (see the preceding paper). Section IV discusses the reduction of the magnitudes of the $\mathbf{a}_q^{(k)}(p)$ as a function of k owing to hyperfine depolarization, and presents the appropriate correction factors. The experimental results are presented in Sec. V, and the physical interpretation of these results are discussed in Sec. VI.

II. EXPERIMENT

The experimental apparatus and techniques have been described elsewhere,[8–10] and a brief overview is given here. Molecular chlorine (Matheson Gases, 99.999%), or the vapor of ICl (Aldrich, 98%), are diluted in a helium carrier gas (Liquid Carbonic, 99.995%) and coexpanded through a pulsed nozzle (General Valve 9-Series, 0.6 mm orifice) into the vacuum chamber from a backing pressure between 200 and 500 Torr. The ICl is photolyzed with linearly polarized light in the 490–560 nm range. The Cl_2 is photolyzed with linearly polarized light at 320 and 470 nm. The 470–560 nm photolysis light is generated from the output of a Nd^{3+}:YAG-pumped tunable dye laser (Continuum PL9020 and ND6000), whereas the 320 nm light is generated from this frequency-doubled output. The photolysis wavelength is calibrated with an iodine spectrum, and the wavelength is known to better than 0.1 nm. The photolysis light is gently focused into the detection region. After 20 ns the Cl$(^2P_{3/2})$ atom photofragments are detected via $(2+1)$ REMPI through the $3p^4\,4p\,^2S_{1/2}$ level. The 20 ns delay is used to ensure that the photolysis and probe lasers are not temporally overlapped to avoid two-color multiphoton processes. The linearly polarized 235 nm probe light (100 μJ/pulse, 6 ns pulse width) is generated from the frequency-doubled output of a Nd^{3+}:YAG-pumped tunable dye laser (Spectra-Physics DCR 2A and PDL-3; Exciton, Coumarin 480 dye), and the beam intersects the ionization region at the focus of a 1.1 m lens. The $^{35}Cl^+$ and $^{37}Cl^+$ ions are detected with a Wiley–McLaren time-of-flight mass spectrometer operated under velocity-sensitive conditions.

The photolysis and probe laser beams counterpropagate perpendicular to the time-of-flight axis. The probe linear polarization is flipped on a shot-to-shot basis to be either parallel or perpendicular to the time-of-flight axis. The polarization flipping is effected by synchronization to the stress cycle of a photoelastic modulator (Hinds International, PEM-80), and the resulting polarizations have a transmittance ratio of at least 256:1 through a linear polarizer. We frequently performed *in situ* measurements to confirm that the polarization flipping did not adversely affect the laser beam power or properties in a biased manner. These measurements consisted of detecting unaligned contaminant HCl, which showed that the signal intensities varied by less than 1% between the two polarization states.

For the measurements of orientation moments, a quarter-wave plate is placed after the photoelastic modulator with its optical axis at 45° to either linear probe polarization. This setup produces right and left circularly polarized light on a shot-to-shot basis. We refer to the time-of-flight profiles from a particular geometry as $\mathbf{I}_G^F$, where F refers to the geometry of the photolysis polarization and G refers to the geometry of the probe polarization. For these experiments, the laboratory Z axis lies along the time-of-flight axis and the Y axis lies along the photolysis propagation direction. A sign indicates the direction of circular polarization, whereas a lack of sign indicates linear polarization. For example, for the $\mathbf{I}_{+Y}^X$ profile, the photolysis laser is linearly polarized along the X axis and the probe laser is right-circularly polarized along the Y axis. For linearly polarized probe light, the isotropic and anisotropic profiles are defined as $\mathbf{I}_{\mathrm{iso}}^F=\mathbf{I}_Z^F+2\mathbf{I}_X^F$ and $\mathbf{I}_{\mathrm{aniso}}^F=\mathbf{I}_Z^F-\mathbf{I}_X^F$, whereas for circularly polarized probe light these profiles are defined as $\mathbf{I}_{\mathrm{iso}}^F=\mathbf{I}_{-Y}^F+\mathbf{I}_{+Y}^F$ and $\mathbf{I}_{\mathrm{aniso}}^F=\mathbf{I}_{-Y}^F-\mathbf{I}_{+Y}^F$.

III. POLARIZATION PARAMETER DETECTION SENSITIVITIES

The values of the polarization parameter detection sensitivities s_k from Eq. (16) of the preceding paper must be calculated so that the absolute values of the $\mathbf{a}_q^{(k)}(p)$ can be obtained. References describing general methods for calculating the s_k are given in the preceding paper. In this paper, we are concerned with detecting photofragments with small J. When J is small, and for carefully chosen spectral transitions in the detection step, the calculation of the s_k is greatly simplified.

In this study, the detection of Cl$(^2P_{3/2})$ photofragments (from a pure perpendicular transition) via $(2+1)$ REMPI using the $3p^4\,4p\,^2S_{1/2}$ intermediate state. The ground state possesses the m states $\pm 3/2$ and $\pm 1/2$, whereas the excited state possesses the $\pm 1/2$ m states only. For a ground state distribution described by the $\mathbf{a}_0^{(2)}(\perp)$ parameter only, and for the probe polarization parallel to the recoil direction ($\Theta=0$), the ionization probability [Eq. (18) of the companion paper] is given by

$$I=1+s_2\mathbf{a}_0^{(2)}(\perp). \tag{1}$$

The use of linearly polarized light only allows transitions for which m does not change ($\Delta m = 0$). If the ground state is populated exclusively in the $\pm 3/2$ states, then transition to the excited state is forbidden (because $m = \pm 3/2$ states do not exist in the excited state). Such a ground state population gives $I = 0$ for Eq. (1), and is described by $\mathbf{a}_0^{(2)}(\perp) = 0.8$ [see Eqs. (28) and (29) of the companion paper]. Solving for s_2 gives $s_2 = -5/4$. Notice that although the value of s_2 was determined from a particular ground-state m-state distribution, this value of s_2 can be used for all $k = 2$ parameters describing any $J = 3/2$ m-state distribution detected via a $J' = 1/2$ excited state using linearly polarized probe light. In a similar fashion, the s_k are calculated for the Cl-atom detection scheme used in this paper and are given by $s_1 = -2\sqrt{5/3}$, $s_2 = -5/4$, and $s_3 = \sqrt{15/4}$. Note that the values of s_k of even k are for linearly polarized probe light, whereas the values of s_k of odd k are for circularly polarized probe light.

IV. HYPERFINE DEPOLARIZATION

The total angular momentum **F** of a Cl atom is the vector sum of the electronic angular momentum **J** and the nuclear angular momentum **I** of the Cl nucleus ($\mathbf{I}_{\mathrm{Cl}} = 3/2$ for both isotopes of chlorine). In these experiments, the bandwidth of our probe laser is much broader than the hyperfine splitting that results from the coupling of **J** with the nuclear spins. Therefore, we detect individual values of J without resolving the hyperfine states. This procedure causes the observed distribution of **J** to be affected in a time-dependent manner by the precession of **J** about **F**. The polarization parameters describing the distribution of **J** oscillate as a function of time about a reduced value. In these experiments, the periods of oscillation are much faster than the temporal widths of the lasers; therefore, these oscillations cannot be observed, and the experiments are sensitive to reduced values of the polarization parameters. This reducing factor is given by[11]

$$\langle G_c^{(k)} \rangle_{\mathrm{av}} = \frac{1}{2I+1} \sum_F (2F+1)^2 \begin{Bmatrix} F & F & k \\ J & J & I \end{Bmatrix}. \qquad (2)$$

For $J = 3/2$, the factor is 0.5 for $k = 1$ and 0.27 for $k = 2$. The measured polarization parameters of particular k are divided by these factors.

V. RESULTS

A. Photodissociation of Cl_2

For the energies used in the photodissociation experiments of Cl_2, two asymptotic channels are accessible. The $C\,^1\Pi_{1u}$ state is accessed via a perpendicular transition and correlates to two $Cl(^2P_{3/2})$ atoms (Cl+Cl), and the $B\,^3\Pi^+_{0\,u}$ state is accessed via a parallel transition and correlates to $Cl(^2P_{3/2})$ and $Cl(^2P_{1/2})$ atoms (Cl+Cl*).[12,13] Hereafter we shall refer to ground-state $Cl(^2P_{3/2})$ and excited-state $Cl(^2P_{1/2})$ atoms as Cl and Cl*, respectively. Previous measurements in the 300–400 nm region have shown that the Cl+Cl channel produces a spatial anisotropy parameter β very close to the limiting value of -1, indicating adiabatic dissociation via the C state.[13,14] In contrast, the Cl+Cl* channel shows approximately $\beta = -1$ at 300 nm and switches to approximately $\beta = +2$ at 370 nm.[13,14] This behavior indicates that at 300 nm the Cl+Cl* channel is populated by nonadiabatic dissociation from the C state, whereas at longer wavelengths this channel is populated by adiabatic dissociation from the B state.

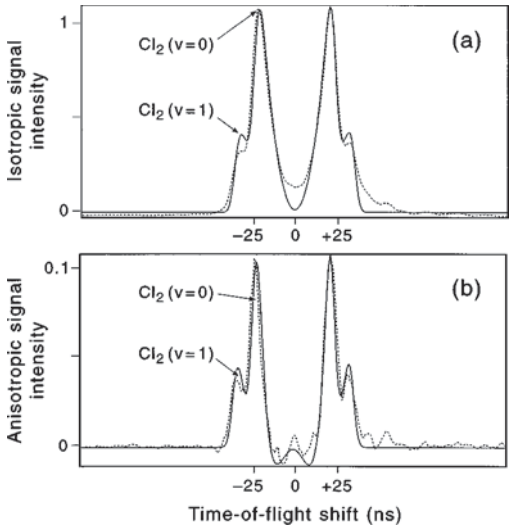

FIG. 1. (a) The isotropic core-extracted $^{35}Cl^+$ ion-arrival composite profile, $\mathbf{I}^Z_{\mathrm{ISO}}$, from the photodissociation of Cl_2 at 470 nm, which is sensitive to the Cl photofragment speed distribution. The photolysis polarization lies along the time-of-flight axis. Notice the fast photofragments from the photodissociation of $v = 1$ Cl_2, and the slower photofragments from the photodissociation of $v = 0$ Cl_2. (b) The anisotropic core-extracted profile, $\mathbf{I}^Z_{\mathrm{aniso}}$, is sensitive to the Cl-photofragment angular momentum distributions. These distributions are described by the $\mathbf{a}_0^{(2)}(\parallel)$ parameter, and analysis of these profiles yields $\mathbf{a}_0^{(2)}(\parallel) \approx -0.7$ for both channels.

1. Photodissociation of Cl_2 via B state at 470 nm

Trends of previous measurements[13,14] suggest that at the dissociation wavelength of 470 nm the Cl+Cl* channel is populated almost exclusively by adiabatic dissociation through the B state. Measurements of the spatial anisotropy are consistent with $\beta = +2$, however, the uncertainty of this measurement cannot rule out small nonadiabatic contributions from the C state. As discussed in the companion paper, dissociations from pure parallel transitions produce photofragments with angular momentum distributions described by the $\mathbf{a}_0^{(k)}(\parallel)$ parameters only [where the notation $(\parallel)$ denotes a pure parallel transition]. Therefore, we expect that the angular momentum distributions of the Cl ($^2P_{3/2}$) atoms from the parallel Cl+Cl* channel should be described by the $\mathbf{a}_0^{(2)}(\parallel)$ parameter only. Pure parallel channels cannot show orientation (only even k), and photofragment $J = 3/2$ restricts $k \leqslant 3$; thus only the $k = 2$ parameter can be nonzero.

The isotropic core-extracted time-of-flight profile, $\mathbf{I}^Z_{\mathrm{iso}}$, for ^{35}Cl atoms is shown in Fig. 1(a). This profile is sensitive to the speed distribution of the Cl atoms. There are at least three distinct channels that contribute to this profile. The two obvious pairs of peaks (symmetric about the zero time-of-flight shift) correspond to Cl atoms from B state dissociation of vibrational ground state ($v = 0$) and vibrationally excited ($v = 1$) Cl_2. The ratio of the intensities of the $v = 1 : v = 0$

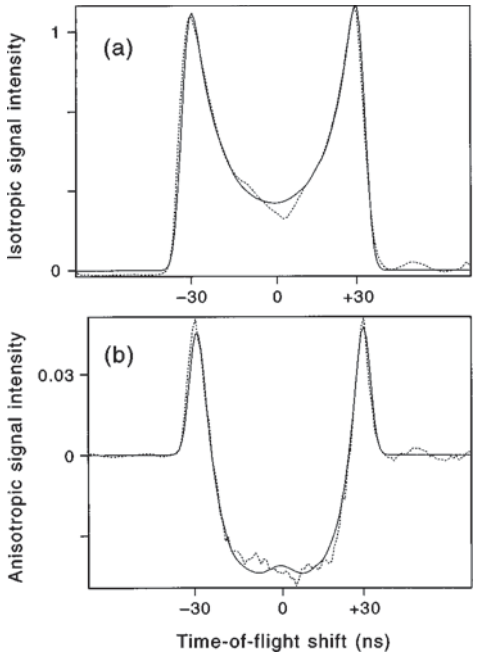

FIG. 2. (a) The isotropic $^{35}Cl^+$ ion-arrival composite profile, $\mathbf{I}^X_{\rm iso}$, from the photodissociation of Cl_2 at 320 nm, which is sensitive to the Cl-photofragment speed distribution. The photolysis polarization lies perpendicular to the time-of-flight axis. This profile shows that the spatial anisotropy of the photofragments is well described by the pure-perpendicular transition limiting value of $\beta=-1$. (b) The anisotropic profile, $\mathbf{I}^X_{\rm aniso}$, is sensitive to the complete Cl-photofragment angular momentum distribution described by the $\mathbf{a}^{(2)}_0(\perp)$ and $\mathbf{a}^{(2)}_2(\perp)$ parameters only. Analysis of these profiles yields $\mathbf{a}^{(2)}_0(\perp)=-0.50$ and $\mathbf{a}^{(2)}_2(\perp)=-0.32$, indicating that the photofragment angular momentum distribution is not cylindrically symmetric about the recoil direction.

states is larger than that expected from the thermal populations indicating that the photodissociation cross section of $v=1$ Cl_2 is enhanced compared to the $v=0$ Cl_2. Notice that the fit fails both in the center of the profiles and on the outer edges. We believe that this deviation is caused by faster Cl atoms from dissociation via the *C* state; these atoms travel preferentially perpendicular to the photolysis polarization (which in this case is parallel to the time-of-flight axis), and we expect that most of these atoms will arrive with small time-of-flight shifts, where the failure of the fit is most evident. The core-extraction technique was used to separate the three contributing channels; also the presence of the Cl atoms from the *C* state was minimized by placing the photolysis polarization parallel to the time of flight.

Figure 1(b) shows the anisotropic time-of-flight profile, $\mathbf{I}^Z_{\rm aniso}$, for the Cl atoms from the Cl+Cl* channel. This profile contains all the information about the Cl atom photofragment polarization. Notice how the $v=1:v=0$ ratio of intensities is similar in both the isotropic and anisotropic profiles, indicating that both channels show similar photofragment polarizations. Analysis of this profile yields $\mathbf{a}^{(2)}_0(\parallel)=-0.7\pm0.2$ for the $v=0$ channel, and $\mathbf{a}^{(2)}_0(\parallel)=-0.6\pm0.2$ for the $v=1$ channel. For $J=3/2$, the physical range of the $\mathbf{a}^{(2)}_0(\parallel)$ parameter is from -0.8 to $+0.8$.

2. Photodissociation of Cl_2 via C state at 320 nm

As mentioned above, at 320 nm Cl_2 dissociates to give two Cl atoms via a perpendicular transition. Figure 2(a) shows the isotropic time-of-flight profile, $\mathbf{I}^X_{\rm iso}$ of the ^{35}Cl atoms. This time-of-flight profile is similar to a Doppler profile and can be fit with a spatial anisotropy parameter $\beta=-1$. The anisotropic time-of-flight profile, $\mathbf{I}^X_{\rm aniso}$, is shown in Fig. 2(b). This profile is sensitive to the photofragment polarization. Since the Cl+Cl channel is produced almost exclusively via a perpendicular transition, we expect the Cl atom photofragment polarization to be described by the $\mathbf{a}^{(2)}_0(\perp)$ and $\mathbf{a}^{(2)}_2(\perp)$ parameters only. The anisotropic profile is fit extremely well with these two parameters to yield $\mathbf{a}^{(2)}_0(\perp)=-0.50\pm0.10$ and $\mathbf{a}^{(2)}_2(\perp)=-0.32\pm0.06$. Fits including the $\mathrm{Re}[\mathbf{a}^{(2)}_1(\parallel,\perp)]$ parameter yield a value of zero for this parameter, indicating that there is not a significant contribution to the alignment from the *B* state.

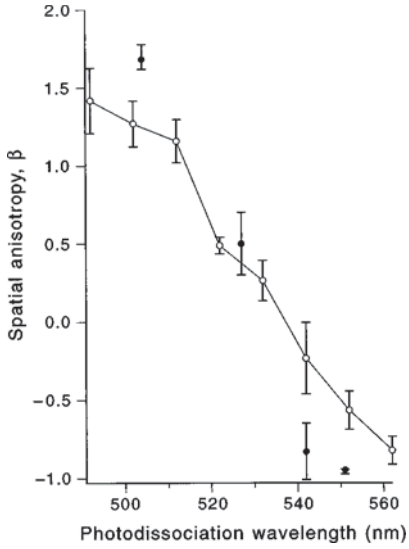

FIG. 3. Measurement of the Cl-photofragment spatial anisotropy parameter β from the photodissociation of ICl with linearly polarized light in the 490–560 nm range (open circles). Notice that this parameter ranges from close to the limiting values of $\beta=+2$ at 490 nm to $\beta=-1$ at 560 nm. This indicates that the dissociation of ICl proceeds predominantly via a parallel transition (through the *B* state) at 490 nm and predominantly via a perpendicular transition (through the *A* state) at 560 nm. The dark circles are predictions of the spatial anisotropy parameter derived from the envelope of the oscillations of the $\mathrm{Im}[\mathbf{a}^{(1)}_1(\parallel,\perp)]$ parameter (see text).

B. Photodissociation of ICl

In these experiments, ICl is photodissociated in the 490–590 nm region. Unlike the two limiting cases observed for Cl_2 at 470 and 320 nm involving single-surface dissociations, ICl dissociates via multiple surfaces in this wavelength region. Figure 3 shows spatial anisotropy measurements in this wavelength region. Notice how the dissociation proceeds from a strongly parallel transition at 490 nm (via the $B\,^3\Pi_{0^+u}$ state) to a strongly perpendicular transition at 560 nm (via the $A\,^3\Pi_{1u}$ state).[15] It is the mixed nature of this transition that allows the presence in the photofragment angular momentum distribution of the interference terms $\mathrm{Im}[\mathbf{a}^{(1)}_1(\parallel,\perp)]$ and $\mathrm{Re}[\mathbf{a}^{(2)}_1(\parallel,\perp)]$, as well as the single-surface terms discussed above, $\mathbf{a}^{(2)}_0(\parallel)$, $\mathbf{a}^{(2)}_0(\perp)$, and $\mathbf{a}^{(2)}_2(\perp)$. The alignment parameters with $k=2$ are probed

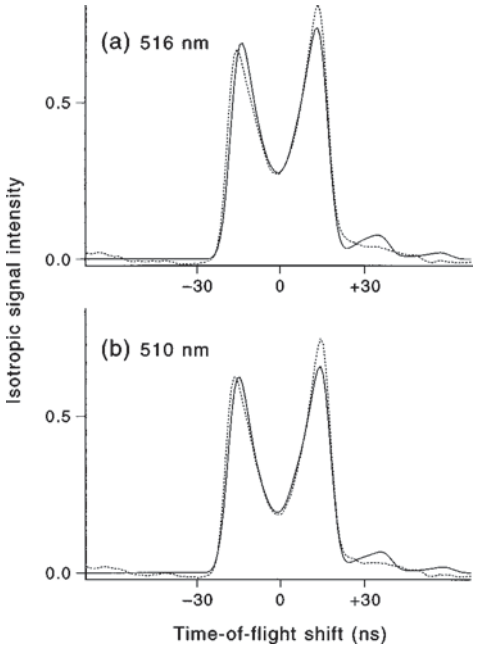

FIG. 4. (a) The isotropic $^{37}Cl^{+}$ ion-arrival composite profile, $\mathbf{I}^{Z}_{iso}$, from the photodissociation of ICl at 516 nm and (b) at 510 nm. Notice that the profiles are very similar; the profile at 510 nm is somewhat more dipped in the center than the profile at 516 nm, as β at this frequency is somewhat more positive. Other than this, there are no large changes in the speed distribution.

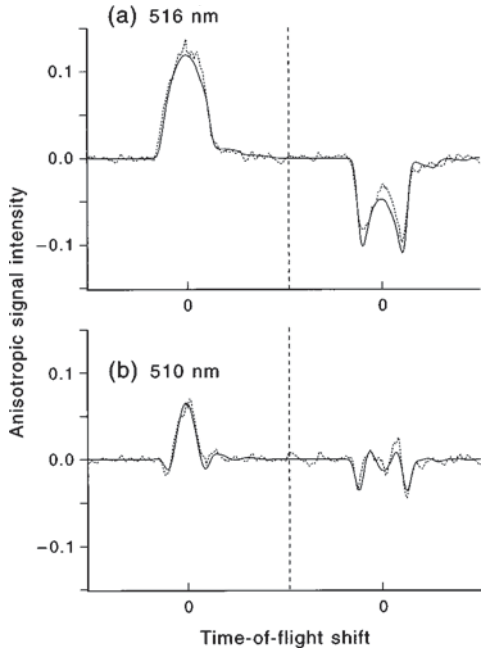

FIG. 5. (a) The anisotropic profiles $\mathbf{I}^{X}_{aniso}$ and $\mathbf{I}^{Z}_{aniso}$ of the ^{37}Cl photofragments from the photodissociation of ICl at 516 nm and (b) 510 nm. These pairs of composite profiles are sensitive to the complete alignment of the ^{37}Cl photofragment angular momentum distributions described by the four polarization parameters of $k=2$ (see text). Notice how dramatically the anisotropic signals sensitive to photofragment alignment change between photodissociation wavelengths of 516 and 510 nm, in strong contrast to the isotropic signals shown in Fig. 4.

with linearly polarized probe light, and the orientation parameter with $k=1$ is probed with circularly polarized probe light.

1. Cl-atom alignment

Recent work in this laboratory measured the $\mathbf{a}^{(2)}_0(\parallel)$, $\mathbf{a}^{(2)}_0(\perp)$, $\mathrm{Re}[\mathbf{a}^{(2)}_1(\parallel,\perp)]$, and $\mathbf{a}^{(2)}_2(\perp)$ alignment parameters for the ^{35}Cl and ^{37}Cl photofragments from the photodissociation of ICl at 532 nm.[16] These measurements showed that the three incoherent single-surface terms are mass independent whereas the $\mathrm{Re}[\mathbf{a}^{(2)}_1(\parallel,\perp)]$ interference term was different for ^{35}Cl and ^{37}Cl. The experiments described in this section are an extension of that work; here we present the alignment of the Cl photofragments at photodissociation wavelengths of 504, 510, 516, and 522 nm, in addition to 532 nm.

Figure 4 presents the isotropic time-of-flight profiles, $\mathbf{I}^{Z}_{iso}$ for ^{37}Cl at photodissociation wavelengths of 510 and 516 nm. Notice that these forms are very similar; the profile at 510 nm possesses a deeper dip in the center because the spatial anisotropy is somewhat more positive at this wavelength (see Fig. 3). As discussed elsewhere,[4,16] the measurement of all four $k=2$ alignment parameters with linearly polarized light requires at least two different photolysis geometries so that the contributions of the four parameters are linearly independent. Figure 5 shows the two anisotropic profiles $\mathbf{I}^{X}_{aniso}$ and $\mathbf{I}^{Z}_{aniso}$ for the ^{37}Cl photofragments at 510 and 516 nm. These profiles contain all the information about the alignment of the ^{37}Cl photofragments. In sharp contrast to the isotropic profiles, notice how different the anisotropic profiles are between photolysis wavelengths 510 and 516 nm, both in shape and magnitude. Just as recent work showed that Cl photofragment alignment depends strongly on the photofragment mass, here we show that the Cl photofragment alignment depends strongly on the photodissociation wavelength. The anisotropic forms shown in Fig. 5, as well as the anisotropic forms for the other wavelengths and for ^{35}Cl, can be analyzed using the methods discussed in the preceding paper to obtain the four $k=2$ alignment parameters. Figure 6 shows the results of this analysis: the wavelength dependence of the ^{35}Cl and ^{37}Cl photofragment alignment. Notice that, within experimental error, the three incoherent alignment parameters, $\mathbf{a}^{(2)}_0(\parallel)$, $\mathbf{a}^{(2)}_0(\perp)$, and $\mathbf{a}^{(2)}_2(\perp)$, are approximately constant as a function of dissociation wavelength. In sharp contrast, the coherent (interference) alignment parameter, $\mathrm{Re}[\mathbf{a}^{(2)}_1(\parallel,\perp)]$, changes dramatically as a function of photodissociation wavelength. This variation ranges both positively and negatively to about 2/3 of the maximal physical value of the $\mathrm{Re}[\mathbf{a}^{(2)}_1(\parallel,\perp)]$ parameter. Therefore the large variations in the photofragment alignment, evident in the signal shown in Fig. 5, arise exclusively from the changes in the $\mathrm{Re}[\mathbf{a}^{(2)}_1(\parallel,\perp)]$ interference term.

2. Cl-atom orientation

Photofragment orientation is probed using circularly polarized probe light. When using linearly polarized photolysis light, photofragment orientation, described by the $\mathrm{Im}[\mathbf{a}^{(1)}_1(\parallel,\perp)]$ parameter, can only arise from interference between dissociating states accessed by at least one parallel and perpendicular transition. The observation and explana-

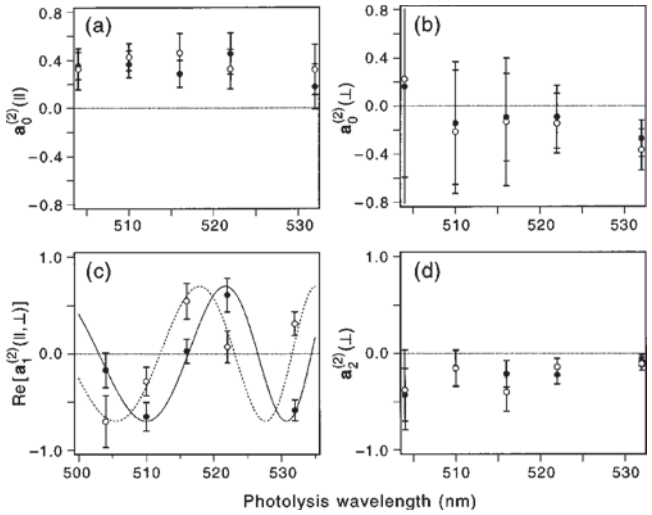

FIG. 6. The 504–532 nm wavelength dependence of the $\mathbf{a}_0^{(2)}(\parallel)$, $\mathbf{a}_0^{(2)}(\perp)$, $\mathrm{Re}[\mathbf{a}_1^{(2)}(\parallel,\perp)]$, and $\mathbf{a}_2^{(2)}(\perp)$ parameters describing the complete ^{35}Cl and ^{37}Cl photofragment alignment from the photodissociation of ICl (shown by the dark and open circles respectively). Notice that, within experimental error, the three incoherent contributions to the alignment, the $\mathbf{a}_0^{(2)}(\parallel)$, $\mathbf{a}_0^{(2)}(\perp)$, and $\mathbf{a}_2^{(2)}(\perp)$ parameters, are approximately constant as a function of dissociation wavelength. In sharp contrast, the coherent contribution to the photofragment alignment, the $\mathrm{Re}[\mathbf{a}_1^{(2)}(\parallel,\perp)]$ interference term, vary dramatically. The solid and dashed lines are the predictions of $\cos\Delta\phi$ for ^{35}Cl and ^{37}Cl, respectively, offset by -2 nm (see text). The agreement between the oscillations of $\mathrm{Re}[\mathbf{a}_1^{(2)}(\parallel,\perp)]$ and $\cos\Delta\phi$ are excellent.

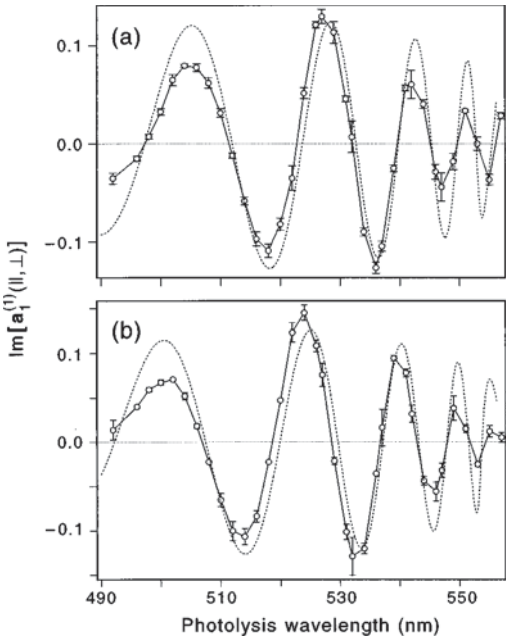

FIG. 7. The 490–560 nm wavelength dependence of the $\mathrm{Im}[\mathbf{a}_1^{(1)}(\parallel,\perp)]$ parameter describing the (a) ^{35}Cl and (b) ^{37}Cl photofragment orientation from the linearly polarized photodissociation of ICl. The dashed lines are the predictions of $\sin\Delta\phi$ for ^{35}Cl and ^{37}Cl (see text); the amplitude of the $\sin\Delta\phi$ plots are multiplied by an envelope calculated from the spatial anisotropy measurements shown in Fig. 3. The actual, more pronounced, experimental envelope is inverted to predict β as a function of wavelength as discussed in the text and shown in Fig. 3.

tion of wavelength-dependent oscillations in Cl photofragment orientation from the photodissociation of ICl was reported recently.[7] The oscillations in the $\mathrm{Im}[\mathbf{a}_1^{(1)}(\parallel,\perp)]$ orientation parameter for both ^{35}Cl and ^{37}Cl are shown here again in Fig. 7 so that detailed features of these oscillations can be discussed.

VI. DISCUSSION

A. Photodissociation of Cl_2 via *B* state at 470 nm

Measurements show that the dissociation of $v=0$ and $v=1$ Cl_2 molecules yield Cl atoms from the Cl+Cl* channel with alignments described by values $\mathbf{a}_0^{(2)}(\parallel)$ very close to the limiting value of -0.8. Using Eqs. (30) and (31) of the companion paper, we see that the value of $\mathbf{a}_0^{(2)}(\parallel)=-0.8$ for $J=3/2$ corresponds to population of the $m_{\mathrm{Cl}}=\pm 1/2$ states only (where the quantization axis is given by the recoil direction). Therefore, these measurements show that the dissociation via the Cl+Cl* channel produces Cl atoms that populate $m_{\mathrm{Cl}}=\pm 1/2$ states almost exclusively.

The excitation of the *B* state occurs via a parallel transition, so that the projection of the total angular momentum along the bond axis of the excited molecule is zero ($\Omega=0$). The angular momenta of the Cl+Cl* photofragments must conserve this projection, so that $m_{\mathrm{Cl}}+m_{\mathrm{Cl}*}=0$. Since $J_{\mathrm{Cl}*}=1/2$, $m_{\mathrm{Cl}*}=\pm 1/2$ only, from which it follows that $m_{\mathrm{Cl}}=\pm 1/2$ only. Thus $\mathbf{a}_0^{(2)}(\parallel)$ is constrained to be -0.8. Therefore, the experimental measurement of the $\mathbf{a}_0^{(2)}(\parallel)$ is within error of the expected value, and represents a test of our experimental techniques and analysis.

B. Photodissociation of Cl_2 via *C* state at 320 nm

The measurement of large nonzero values of $\mathbf{a}_0^{(2)}(\perp)=-0.50$ and $\mathbf{a}_2^{(2)}(\perp)=-0.32$ indicate that the Cl atoms from *C*-state dissociation are highly aligned. Also, the large value of the $\mathbf{a}_2^{(2)}(\perp)$ indicates that photofragment angular momentum distributions are not cylindrically symmetric with respect to the recoil direction. Using Eq. (8) of the preceding paper and these polarization-parameter values, the Cl-atom photofragment angular momentum distribution is plotted in Fig. 8(a) with respect to $\mathbf{v}$ and μ. Notice that this spatial distribution is strongly peaked parallel to the y axis (perpendicular to both $\mathbf{v}$ and μ). Expressing this distribution with the y axis as the quantization axis gives $\mathbf{a}_0^{(2)}(y)=+0.64$ and $\mathbf{a}_2^{(2)}(y)=-0.15$. This near-maximal value of the $\mathbf{a}_0^{(2)}(y)$ implies that the $m_y=\pm 3/2$ states are 90% populated, and the $m_y=\pm 1/2$ states are only 10% populated [see Eqs. (30) and (31) in the preceding paper]. Figure 8(b) shows the angular distribution of the $m_y=\pm 3/2$ states. Comparison of the experimentally derived plots of Fig. 8(a) with the maximal *m*-state distribution of Fig. 8(b) shows them to be very similar, illustrating that the Cl atoms are very strongly aligned perpendicular to the plane defined by $\mathbf{v}$ and μ.

A possible interpretation of this strong alignment is a simple model that considers only the electronic orbital angular momentum and neglects the electronic spin. As such, this model does not provide an exact description and is only presented to aid in the physical understanding of the observed alignment effects. The transition from the ground state to the *C* state promotes an electron from a π^* to a σ^* molecular

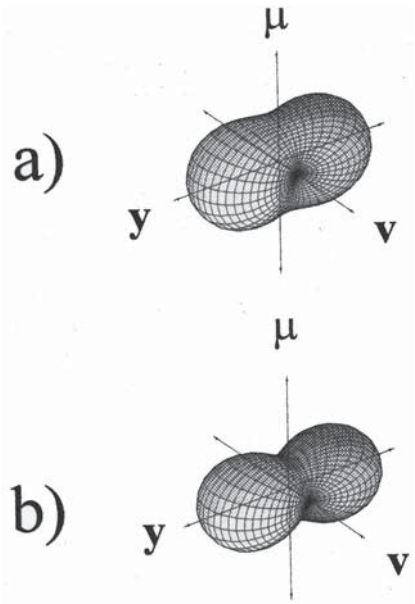

FIG. 8. (a) Plots of the Cl-photofragment angular momentum distributions from the photodissociation of Cl_2 at 320 nm. Notice that the $J=3/2$ angular momentum is strongly peaked perpendicular to both the recoil direction $\hat{\mathbf{v}}$ and the transition dipole moment μ. (b) A plot of the $m_y=\pm 3/2$ distribution, showing the strong similarity with the experimental measurement, and that the measured Cl atoms are nearly maximally aligned with respect to the y axis.

orbital. In the atomic orbital picture, an electron is being promoted from a p_x to a p_z orbital. Since the two Cl atoms are equivalent, each of the two unpaired electron occupies a $p_x \pm i p_z$ orbital so that the wave functions of the two electrons are orthogonal. This occupation of orbitals corresponds to an m-state distribution of the $L=1$ orbital angular momentum of $m_y=\pm 1$ for each atom; also the m states of the paired atoms are correlated so that a measurement of $m_y=+1$ for one atom will correlate to $m_y=-1$ for its pair. Therefore, following excitation, the orbital angular momentum is maximally aligned perpendicular to $\mathbf{v}$ and μ. If the electronic spin were to couple parallel to the electronic orbital angular momentum, we would obtain $m_y=\pm 3/2$ for each atom, very similar to that observed. The slight disagreement of the experimental observation with this picture may be due to the nature of the spin-orbit coupling; the coupling of L and S parallel to the bond may be different for that perpendicular to the bond, thus breaking cylindrical symmetry of J about the y axis.

Overall, we conclude that the Cl-atom alignment is consistent with the adiabatic dissociation of Cl_2 molecules via the C state. In other recent experiments, Bracker *et al.*[17] measured the Cl-atom alignment from the dissociation of Cl_2 via the C state at 355 nm using the ion imaging technique. The absolute alignment was not measured, but a quantity equal to $[\mathbf{a}_0^{(2)}(\perp)/\mathbf{a}_2^{(2)}(\perp)]$ was reported to be 1.5; our value of 1.56 ± 0.3 for this ratio is in excellent agreement with this independent measurement.

C. Photodissociation of ICl

The $\mathbf{a}_0^{(2)}(\parallel)$ parameter describes the Cl angular momentum distribution from the B-state (parallel) dissociation of

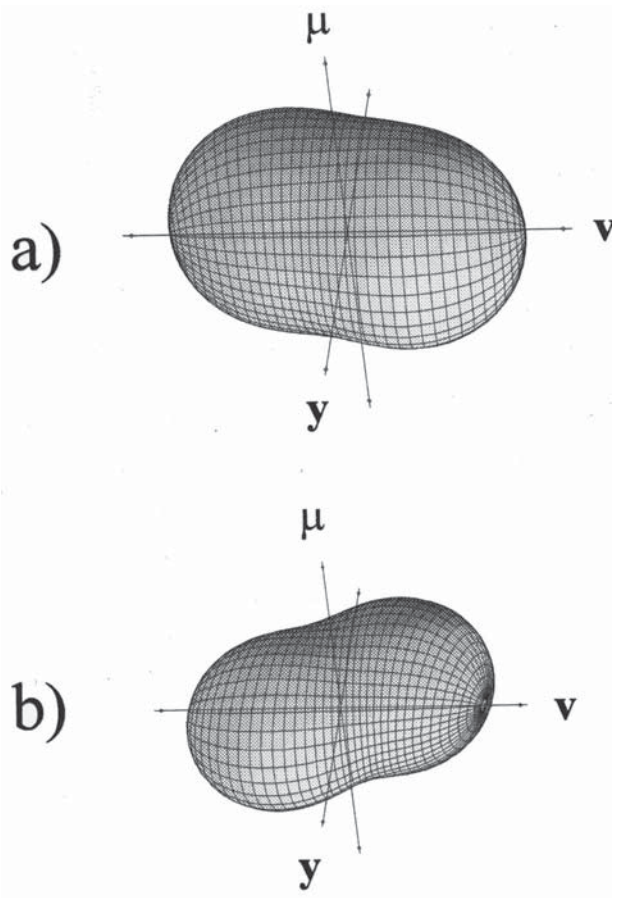

FIG. 9. (a) Plot of the complete angular momentum distribution for the ^{37}Cl photofragments from the photodissociation of ICl at 516 nm and (b) 510 nm. The photolysis polarization lies 45° to the recoil direction.

ICl, and contains information about the dynamics of this dissociation process. The $\mathbf{a}_0^{(2)}(\perp)$ and $\mathbf{a}_2^{(2)}(\perp)$ parameters describe the Cl angular momentum distribution from the A-state (perpendicular) dissociation of ICl, and they contain information about the dynamics of this dissociation process. The single-surface dynamics on these two surfaces are unrelated to each other (incoherent), and so measuring these parameters simultaneously (in experiments in which both surfaces are coherently excited) yields the same values when they are measured separately (in experiments in which the surfaces are incoherently excited). The advantage of coherently exciting the A and B states is the additional presence of the $\mathrm{Im}[\mathbf{a}_1^{(1)}(\parallel,\perp)]$ and $\mathrm{Re}[\mathbf{a}_1^{(2)}(\parallel,\perp)]$ interference parameters in the Cl angular momentum distribution. These parameters contain information about the relative phase difference between the asymptoptic wavefunctions, and are thus sensitive to the shapes of the surfaces. The Cl angular momentum distributions from the photodissociation of ICl in the 490–560 nm region can be described by all five of the polarization parameters mentioned above, and as such this dissociation is ideal for illustrating the usefulness of the $\mathbf{a}_q^{(k)}(p)$ formalism.

Figure 9 shows plots of the ^{37}Cl-atom angular momentum distributions at dissociation wavelengths of 510 and 516 nm. At first sight, the Cl-atom photofragment polarization seems complicated; the physical meaning of these distributions is not readily apparent. These distributions can, of

course, be expressed in terms of the $\mathbf{a}_q^{(k)}(p)$ polarization-parameter formalism. We see that of the five parameters, only the two $\mathbf{a}_1^{(k)}(\parallel,\perp)$ are changing with photodissociation wavelength and photofragment mass (see Figs. 6 and 7). As mentioned in the companion paper, the $\mathrm{Im}[\mathbf{a}_1^{(1)}(\parallel,\perp)]$ parameter is proportional to $\sin\Delta\phi$ and the $\mathrm{Re}[\mathbf{a}_1^{(2)}(\parallel,\perp)]$ parameter is proportional to $\cos\Delta\phi$ (where $\Delta\phi$ is the phase difference between the asymptotic continuum wavefunctions associated with interfering surfaces accessed by parallel and perpendicular transitions; this phase difference depends on excitation wavelength and photofragment mass). In contrast, the incoherent polarization parameters appear to be approximately constant in this region.

Together, these polarization parameter values can be used to form a very simple picture of the dissociation process. The dissociation dynamics on either surface does not depend (or depends very weakly) on the excitation wavelength or the photofragment mass. However, the total contribution from each surface is changing with wavelength as the β parameter changes monotonically with wavelength (Fig. 3), so that at 490 nm the dissociation occurs predominantly via the *B* state whereas at 560 nm the dissociation occurs predominantly via the *A* state. Also, the interference contributions to the photofragment polarization, the $\mathrm{Im}[\mathbf{a}_1^{(1)}(\parallel,\perp)]$ and $\mathrm{Re}[\mathbf{a}_1^{(2)}(\parallel,\perp)]$ parameters, oscillate sinusoidally with excitation wavelength in a fashion that is sensitive to the shapes of the dissociative surfaces. Therefore, although various observables such as the photofragment polarization and spatial anisotropy are changing rapidly with excitation wavelength (and these variations are rich in information about dissociative surface shapes), the actual single-surface dissociation dynamics are not changing.

The interference of two dissociative states accessed by transitions of different symmetry is analogous to a variant of Young's double-slit experiment, with two slits transmitting perpendicular polarizations (see Fig. 10). If the light used is initially linearly polarized, and crossed polarizers are placed in front of the two slits (at 45° to the linear polarization so that both slits transmit equally), then the light on the screen will show a polarization fringe pattern (instead of the usual intensity fringe pattern). The polarization, $\hat{\mathbf{p}}$, at some point on the screen will be elliptical in general, and will be described by

$$\hat{\mathbf{p}}=\frac{1}{\sqrt{2}}(\hat{\mathbf{x}}+e^{i\Delta\phi}\hat{\mathbf{y}}), \tag{3}$$

where $\hat{\mathbf{x}}$ and $\hat{\mathbf{y}}$ are parallel to the vertical and horizontal, respectively, and $\Delta\phi$ is the phase difference between the two pathways. This polarization pattern can be separated into components very similar to the $\mathbf{a}_q^{(k)}(p)$. If the pattern is probed with a linear polarizer that is vertical or horizontal, then the $\Delta\phi$-independent envelope with no oscillations shown at top will be seen (in analogy to the $\Delta\phi$-independent incoherent
$\mathbf{a}_0^{(2)}(\parallel)$, $\mathbf{a}_0^{(2)}(\perp)$, and $\mathbf{a}_2^{(2)}(\perp)$ parameters). If the pattern is probed with a linear polarizer at $+45°$ and separately at $-45°$, and these two signals are subtracted, then the $\cos\Delta\phi$ interference pattern shown in the middle is seen (in analogy to the coherent $\mathrm{Re}[\mathbf{a}_1^{(2)}(\parallel,\perp)]$ term). Finally, if the pattern is probed with a right and a left circularly polarizer and these two signals are subtracted, then the $\sin\Delta\phi$ interference pattern shown at the bottom is seen (in analogy to the coherent $\mathrm{Im}[\mathbf{a}_1^{(1)}(\parallel,\perp)]$ term).

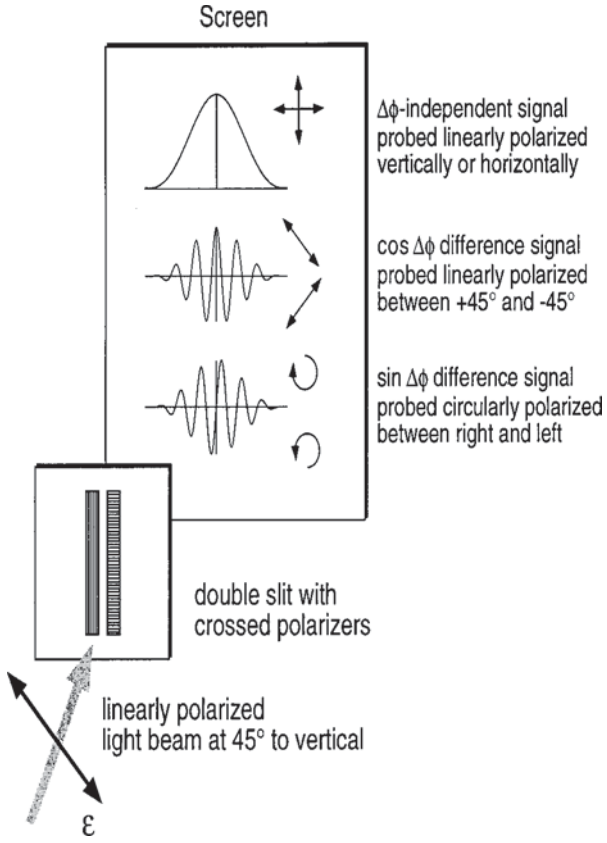

FIG. 10. Variant of Young's double-slit experiment. The light beam is initially linearly at 45° to vertical, and crossed polarizers are placed in front of the two slits, producing a polarization interference pattern on the screen. The polarization pattern can be probed with linear and circular polarizers. The pattern at top is produced when a linear polarizer is placed either vertically or horizontally in front of the screen, and is $\Delta\phi$ independent (analogous to the incoherent alignment parameters). The pattern in the middle is the difference between patterns produced by a linear polarizer placed at 45° and separately at $-45°$ to vertical, and varies as $\cos\Delta\phi$ (analogous to $\mathrm{Re}[\mathbf{a}_1^{(2)}(\parallel,\perp)]$). The pattern at the bottom is the difference between patterns produced by right and left circular polarizers, and varies as $\sin\Delta\phi$ (analogous to $\mathrm{Im}[\mathbf{a}_1^{(1)}(\parallel,\perp)]$).

Solution of the one-dimensional Schrödinger equation as a function of dissociation wavelength for the *ab initio A* and *B* surfaces allows the calculation of the wavelength-dependent asymptoptic phase difference, $\Delta\phi=\phi_A-\phi_B$. In Figs. 6 and 7, $\mathrm{Re}[\mathbf{a}_1^{(2)}(\parallel,\perp)]$ is compared to $\cos\Delta\phi$ and $\mathrm{Im}[\mathbf{a}_1^{(1)}(\parallel,\perp)]$ is compared to $\sin\Delta\phi$. In Fig. 6, the theoretical prediction of $\cos\Delta\phi$ has been offset by -2 nm to improve the fit. Notice that in Fig. 7, in the 510–530 nm region, the difference between the experiment and theory is also -2 nm, in agreement with Fig. 6. Overall, the agreement between theory and experiment is excellent. We note that the $\mathrm{Re}[\mathbf{a}_1^{(2)}(\parallel,\perp)]$ parameter is much more difficult to measure than the $\mathrm{Im}[\mathbf{a}_1^{(1)}(\parallel,\perp)]$ parameter because the $\mathrm{Re}[\mathbf{a}_1^{(2)}(\parallel,\perp)]$ must be measured simultaneously with the three other incoherent parameters with $k=2$. Both interference parameters contain the same information as one is pro-

portional to $\sin\Delta\phi$ and the other to $\cos\Delta\phi$. Therefore, while it is satisfying that the $\mathrm{Re}[\mathbf{a}_1^{(2)}(\parallel,\perp)]$ oscillates in a fashion consistent with the $\mathrm{Im}[\mathbf{a}_1^{(1)}(\parallel,\perp)]$ oscillations demonstrating the internal consistency of these experiments, we emphasize that the measurement of $\mathrm{Im}[\mathbf{a}_1^{(1)}(\parallel,\perp)]$ parameter is, for experimental reasons, much more sensitive and much more convenient for the determination of $\Delta\phi$. For the $\mathrm{Im}[\mathbf{a}_1^{(1)}(\parallel,\perp)]$ parameter, the experimental error bars are small enough that small discrepancies between experiment and theory can be observed. Notice that there is no theoretical prediction of the envelope of the oscillations. The envelope shown is determined from the measured spatial anisotropy parameter, β, as described below. Therefore, the agreement between experiment and theory is best determined by comparing the locations of the zero crossings. We see that these crossing are accurately predicted everywhere except for slight deviations in the 510–530 nm region. One possible explanation is that the surfaces need to be slightly corrected. Another explanation is that curve crossings may play a role, as discussed by Yabushita.[18] In particular, the *B* state encounters an avoided crossing with another excited dissociative surface at large internuclear separation. Yabushita predicts that the curve-crossing probability is large, and so recrossing to the *B* state would result in an additional phase shift. Such curve-crossing effects would be most noticable at low dissociation energies. Therefore, the effect of curve crossings need to be investigated theoretically before we can conclude that the discrepancies between theory and experiment are exclusively caused by inaccuracies in the surface shape.

As mentioned in the preceding paper, the $\mathbf{a}_1^{(k)}(\parallel,\perp)$ interference terms are proportional to $\sqrt{(1+\beta)(1-\beta/2)}$ for contributions from exactly one parallel and one perpendicular dissociative surface. Notice that there is an envelope to the experimental wavelength-dependent oscillation of the $\mathrm{Im}[\mathbf{a}_1^{(1)}(\parallel,\perp)]$ shown in Fig. 7, and that the envelope is maximal at about 525 nm when $\beta=+0.5$ and the quantity $\sqrt{(1+\beta)(1-\beta/2)}$ is also maximal. Assuming that the envelope arises entirely from the $\sqrt{(1+\beta)(1-\beta/2)}$ term, we can invert the envelope and predict the values of β as a function of wavelength and compare to the observed values. These predictions are shown in Fig. 3. We see that the gross trend of the two measurements are very similar, as they both show that the spatial anisotropy changes from approximately $+2$ to -1 in the 490–560 nm region. The predictions from the experimental envelope, however, have a distinctly steeper slope. In Fig. 7, the envelope imposed upon the theoretical oscillations is derived from the experimental spatial anisotropy measurements. Thus, the comparison of the two envelopes is equivalent to the comparison of the two curves in Fig. 3. We see again that the two measurements are qualitatively similar but are somewhat at odds quantitatively. Possible explanations of this discrepancy include a systematic error in the spatial anisotropy measurements or a breakdown in the assumption that the envelope is well described by $\sqrt{(1+\beta)(1-\beta/2)}$. One reason for such a breakdown would be the presence of a third state in the dissociation. Such a contribution may be occurring from the *C* state below 500 nm, and may help explain the discrepancy in this region.

D. Summary

We have measured the complete molecular-frame Cl ($^2P_{3/2}$) photofragment angular momentum distributions from the single-surface photodissociation of Cl_2 at 320 and 470 nm, and the multiple-surface photodissociation of ICl in the 490–560 nm region. The usefulness of the $\mathbf{a}_q^{(k)}(p)$ formalism is demonstrated by showing how the angular momentum distributions can be decomposed into single-surface and multiple-surface contributions, and by showing the physical significance of this decomposition.

ACKNOWLEDGMENTS

S.A.K. thanks the National Science Foundation for a predoctoral fellowship. S.A.K. also gratefully acknowledges receipt of a Dr. Franklin Veatch Memorial Fellowship. This work has been supported by the National Science Foundation under Grant No. CHE-93-22690.

[1] R. J. van Brunt and R. N. Zare, J. Chem. Phys. **48**, 4304 (1968).
[2] A. T. J. B. Eppink, D. H. Parker, M. H. M. Janssen, B. Buijsse, and W. J. van der Zande, J. Chem. Phys. **108**, 1305 (1998).
[3] L. D. A. Siebbeles, M. Glass-Maujean, O. S. Vasyutinskii, J. A. Beswick, and O. Roncero, J. Chem. Phys. **100**, 3610 (1994).
[4] T. P. Rakitzis and R. N. Zare, J. Chem. Phys. **110**, 3341 (1999), preceding paper.
[5] E. Flemming, G. Reichardt, H. Schmoranzer, and O. Wilhelmi, Phys. Lett. A **192**, 52 (1994).
[6] E. Flemming, O. Wilhelmi, H. Schmoranzer, and M. Glass-Maujean, J. Chem. Phys. **103**, 4090 (1995).
[7] T. P. Rakitzis, S. A. Kandel, A. J. Alexander, Z.-H. Kim, and R. N. Zare, Science **281**, 1346 (1998).
[8] W. R. Simpson, A. J. Orr-Ewing, S. A. Kandel, T. P. Rakitzis, and R. N. Zare, J. Chem. Phys. **103**, 7299 (1995).
[9] S. A. Kandel, T. P. Rakitzis, T. Lev-On, and R. N. Zare, J. Chem. Phys. **105**, 7550 (1996).
[10] T. P. Rakitzis, S. A. Kandel, T. Lev-On, and R. N. Zare, J. Chem. Phys. **107**, 9392 (1997).
[11] R. N. Zare, *Angular Momentum, Understanding Spatial Aspects in Chemistry and Physics* (Wiley–Interscience, New York, 1988).
[12] N. Billy, G. Gouedard, B. Girard, and J. Vigue, J. Phys. II **1**, 323 (1991).
[13] Y. Matsumi, K. Tonokura, and M. Kawasaki, J. Chem. Phys. **97**, 1065 (1992).
[14] P. C. Samartzis, B. Bakker, T. P. Rakitzis, D. H. Parker, and T. N. Kitsopoulos, J. Chem. Phys. (in press).
[15] The potential energy curves of the *A* and *B* states have been calculated by Yabushita, and these surfaces have been published in Ref. 7 with his permission.
[16] T. P. Rakitzis, S. A. Kandel, and R. N. Zare, J. Chem. Phys. **108**, 8291 (1998).
[17] A. S. Bracker, E. R. Wouters, A. G. Suits, Y. T. Lee, and O. S. Vasyutinskii, Phys. Rev. Lett. **80**, 1626 (1998).
[18] S. Yabushita, J. Mol. Struct. (THEOCHEM) (in press).